Mathematical Biosciences and Engineering

MBE, 17(4): 3894−3908.
DOI: 10.3934/mbe.2020216
Received: 09 March 2020
Accepted: 17 May 2020
Published: 25 May 2020

http://www.aimspress.com/journal/MBE

Research article

Conformation and mechanics of the polymeric cuff of artificial urinary sphincter

Arturo Nicola Natali[1,2], Chiara Giulia Fontanella[1,2,*], Silvia Todros[1,2], Piero G. Pavan[1,2], Simone Carmignato[2,3], Filippo Zanini[3] and Emanuele Luigi Carniel[1,2]

[1] Department of Industrial Engineering, University of Padova, Italy
[2] Centre for Mechanics of Biological Materials, University of Padova, Italy
[3] Department of Management and Engineering, University of Padova, Italy

*** Correspondence:** Email: chiaragiulia.fontanella@unipd.it; Tel: +39(0)498276754.

Abstract: The surgical treatment of urinary incontinence is often performed by adopting an Artificial Urinary Sphincter (AUS). AUS cuff represents a fundamental component of the device, providing the mechanical action addressed to urethral occlusion, which can be investigated by computational approach. In this work, AUS cuff is studied with reference to both materials and structure, to develop a finite element model. Materials behavior is investigated using physicochemical and mechanical characterization, leading to the formulation of a constitutive model. Materials analysis shows that AUS cuff is composed by a silicone blister joined with a PET fiber-reinforced layer. A nonlinear mechanical behavior is found, with a higher stiffness in the outer layer due to fiber-reinforcement. The cuff conformation is acquired by Computer Tomography (CT) both in deflated and inflated conditions, for an accurate definition of the geometrical characteristics. Based on these data, the numerical model of AUS cuff is defined. CT images of the inflated cuff are compared with results of numerical analysis of the inflation process, for model validation. A relative error below 2.5% was found. This study is the first step for the comprehension of AUS mechanical behavior and allows the development of computational tools for the analysis of lumen occlusion process. The proposed approach could be adapted to further fluid-filled cuffs of artificial sphincters.

Keywords: artificial urinary sphincter; material characterization; mechanics characterization; micro computed tomography; numerical model

1. Introduction

Severe urinary incontinence (SUI) is currently a widespread healthcare problem with millions of male patients worldwide [1], mostly aged over 50 years [2]. Male patients may undergo surgical treatment with Artificial Urinary Sphincter (AUS). This device ensures continence through occlusion of the urethral duct by means of a cuff generally placed in urethral bulbar region [3]. The most used AUS worldwide is the AMS 800 (Boston Scientific, Boston, USA) (Figure 1a). This prosthesis is based on an inflatable cuff (Figure 1b,c), a pressure-regulating balloon and a pump. Due to the surgical invasiveness of this device and a moderate rate of complications and revisions [3], new solutions have been developed in recent years. These devices are designed to simplify surgical procedures by decreasing the number of connecting parts and to allow the control of the cuff pressure in situ. Indeed, it is recognized that constant urethral pressure is probably causing urethral atrophy and erosion. Among new solutions, other devices present a similar structure and working principle to AMS 800. The ZSI 375 (Zephyr Surgical Implants, Geneva, Switzerland) (Figure 1d) is based on two parts connected by a tube and an adjustable cuff (Figure 1e,f) molded to fit around the urethra, a pressure-regulating reservoir and a pump. The pressure-regulating reservoir operates with a spring-controlled piston mechanism able to move a solution within the hydraulic circuit. The advantages of this device are related to low cost, adjustable cuff pressure and component size minimization. However, clinical trials did not highlight satisfactory results and the device has not been broadly implanted. Another alternative prosthesis is Tape Mechanical Occlusive Device TMOD (GT Urological, Minneapolis, MN, USA) [4], (Figure 1g), based on a spring-loaded mechanism able to move solution up to an occlusive cuff (Figure 1h,i), applying pressure around the urethra. Up to now, TMOD has been studied in a canine model and human cadavers, while clinical trials are in progress. More recent devices include Victo (Promedon, Córdoba, Argentina), which is based on the same working principle of AMS800, showing a modified cuff conformation (Figure 1l) [5,6], and Artus (MyoPowers Medical Technologies France SAS, Besançon, France), based on a smooth segmented silicon cuff that is individually actionable and adjustable with a remote control (Figure 1m). This device has already undergone first clinical studies [5,7] and seems promising due to a combination of new operational concept and optimized cuff design.

Nonetheless, at present AMS 800 remains to be considered the most safe and reliable treatment for stress UI [3,5−10], and is the most frequently used worldwide. Despite positive post-surgery outcomes, a relevant portion of patients requires revision surgery, due to complications including infection, urethral atrophy, erosion, and mechanical failure. These negative side effects are reported in clinical studies but are not investigated from a mechanical point of view. Considering its mechanical behavior, urethral duct is characterized by low stiffness and viscoelastic properties [11,12]. In order to occlude the urethra lumen against the bladder pressure, which can reach values of more than 40 cmH_2O, a well-defined occluding action on the urethra has to be applied. The natural urethral sphincters are two muscles used to control the urine flow out of the bladder. These sphincters are able to guarantee continence for low bladder pressure and to exert a higher occlusive action to support the sudden increase of internal pressure, for example during cough, avoiding incontinence. In case of SUI, such occluding action can be produced by the AUS which must guarantee occlusion during all daily activities. Consequently, the occluding actions are usually elevated and protracted for a long period of time, determining a non-homogeneous strain field within urethral tissues. The value of strain may overcome 30% and can cause inflammation,

atrophy and erosion phenomena. The specific occluding action that is required to close the urethra also depends on the AUS cuff structural conformation, as reported [13,14]. Actually, a successful treatment depends on the mechanical interaction between AUS cuff and urethral tissues.

Figure 1. AUS devices: AMS 800 (a), with details of the deflated (b) and closed inflated cuff (c); ZSI 375 (d), with details of the deflated (e) and inflated cuff (f); TMOD (g), with drawings of the open (h) and closed cuff (i); Victo (l); Artus (m).

AMS 800 cuff is chosen as reference in this work and is characterized by means of physicochemical and mechanical tests, addressed to the definition of a constitutive model of the cuff material. Several geometric configurations of the cuff, respectively deflated and inflated with pressures of 15, 30, and 50 cmH2O, are acquired by Computed Tomography (CT). This technique is increasingly used in geometrical metrology by non-destructive procedures to perform dimensional measurements with high accuracy and is capable for detailed three-dimensional geometrical models reconstruction [15−20]. CT data are assumed for the definition of the numerical model. The model is validated comparing CT images of the inflated cuff and the correspondent numerical results. This numerical model is applied for the investigation of urethral tissues response using AUS by a computational approach [14,21].

2. Materials and methods

2.1. Morphological and physicochemical characterization

The experimental investigation was developed using a cuff provided by Boston Scientific. The sphincteric cuff is made up by a polymeric blister joined with a fiber-reinforced layer. To investigate these materials, morphological and physicochemical analyses were carried out. Preliminarily, the

intact cuff was observed via optical microscopy (ZEISS Stemi 2000-C, Carl-Zeiss, Germany) with an Axio-Cam ERc5s photo camera, aiming at a definition of cuff conformation. Moreover, in order to evaluate cuff surface morphology, concerning both the polymer layer and the fiber-reinforced layer, samples were investigated by means of Environmental Scanning Electron Microscopy (E-SEM, FEI Quanta 200, FEI Company, USA). Energy-Dispersive X-ray Analysis (EDAX), also for an elemental analysis of the components, thus getting a primary evaluation of their chemical composition.

The cuff was cut in portions. Two samples (blister sample: 9 mm × 9 mm; cross section of fiber-reinforced layer: 1.5 mm × 9 mm) were analyzed by Fourier Transform Infrared Spectroscopy (FT-IR) by means of a NicoletTM iSTM 50 FT-IR Spectrometer with built-in ATR (Thermo Fisher Scientific™).

2.2. CT scanning

The metrological CT system (Nikon X-Tek MCT225) equipped with a micro-focus X-ray source, a 16-bit detector with 2000 × 2000 pixels, and a high-precision manipulator is temperature-controlled (20 ± 0.5 ℃) and reaches acceleration voltages of 225 kV [22]. The AMS800 cuff was scanned at air pressures of 0, 15, 30, and 50 cmH2O to evaluate the mechanical response, considering the maximum value reached with the open fluid-filled cuff during experimental activities. The CT measurement procedure consisted of three main steps, as acquisition of bi-dimensional X-ray projections of the sample at homogeneously distributed angular positions between 0 and 360 ° (with angular step equal to 0.24 °), three-dimensional reconstruction of a voxel-based geometrical model and surface determination [22]. To avoid the impact of gravity onto cuff's shape, the sample was placed on a high precision rotary table after being oriented in vertical position using a support made of carbon fiber reinforced polymer, chosen according to low X-ray absorption. The parameters used for CT scanning are reported in Table 1. After the X-ray projections were collected, a 3D virtual solid model of the investigated cuff was reconstructed by means of a filtered back-projection algorithm [23]. The achieved voxel size was 37 μm. The surface determination procedure was performed using the software VGStudio MAX 3.1 (Volume Graphics GmbH, Germany), applying a local adaptive thresholding method in order to define the material boundaries with sub-voxel accuracy [24]. Local adaptive thresholding chooses threshold values for every pixel in the image based on an analysis of its neighboring pixels, as described in [24]. This procedure has been chosen with the final purpose to define a 3D model of AUS cuff.

Table 1. CT scanning parameter.

Parameter	Value
Voltage	150 kV
Current	93 μA
Power	14 W
Exposure time	1000 ms
Nr. of projections	1500

2.3. Mechanical tests

Experimental tests on cuff materials and overall structure, as uniaxial tensile test on samples and overall cuff inflation test, were carried out to evaluate the actual mechanical behavior, as a basis for constitutive modeling. Material mechanical characterization was carried out by a Bose Electro-Force Planar Biaxial Test Bench Instrument, under displacement control with a precision of 0.001 mm and using a load cell with a precision of 0.02 N [11]. Rectangular pieces 3 × 9 mm were cut from the cuff. Their mean width was determined from five independent measurements each. Sample thickness was identified from CT images of the cuff region where each sample was cut. Each test was repeated on three samples, by imposing elongation up to 35% strain, which is the maximum strain value measured in CT images when the cuff is inflated at high pressure. For each experimental test, nominal stress (σ) together with nominal strain (ε) were measured and, for each group of test repetitions, the mean values and standard deviations (SD) were calculated.

The structural behavior of the cuff was analyzed by inflation tests [11,12,25−28] and used for the validation procedure. Details about the inflation protocol are reported as follows [14,21]. Sample experimenting was performed by continuous inflation of saline (0.9% NaCl, room temperature) at 0.5 mL/s inflation rate [21] up to full filling of the cuff, which was achieved at 4 mL. The overall inflation test was repeated three times.

2.4. Numerical model

Data from CT was subsequently elaborated by 3D CAD software (UGS NX 6; Siemens PLM Software, Munich, Germany) to define a virtual solid model. The solid model was discretized into the finite element pre-processing software Abaqus/CAE 6.14 [29]. Different models were developed assuming incremental mesh refinement using 4-node tetrahedral elements. Numerical analyses were performed comparing the results, aiming at a sensitivity analysis with regard to mesh conformation. The final configuration was of about three hundred thousand degrees of freedom providing a numerical model capable of interpreting the mechanical behavior with suitable accuracy and minor computational cost. For the polymeric blister, considering the results from the tensile tests, an isotropic hyperelastic formulation [30] was assumed:

$$W(\mathbf{C}) = C_1\left(\tilde{I}_1 - 3\right) + K_v\left(J-1\right)^2 \tag{1}$$

where $\mathbf{C}$ is the right Cauchy-Green strain tensor, $\tilde{I}_1$ is the first iso-volumetric invariant of $\mathbf{C}$, as $\tilde{I}_1 = \mathrm{tr}\left(J^{-2/3}\mathbf{C}\right)$ and J is the deformation Jacobian, as $J = \sqrt{\det\left(\mathbf{C}\right)}$. The volumetric stiffness is related to the constitutive parameter K_v, as $B = 2K_v$, while shear stiffness is defined as $G = 2C_1$ [30].

The mechanical behavior of the reinforced layer was defined using a fiber-reinforced hyperelastic model based on the contributions of two fibers families along the principal directions of the reinforcing mesh. The following general formulation of the strain energy, divided in the isotropic matrix (W_m) and the fibers (W_f) [31−33] contributions, was defined:

$$W(\mathbf{C}) = W_m\left(\mathbf{C}\right) + W_{f_i}\left(\mathbf{C}, \mathbf{a}_0{}^i \otimes \mathbf{a}_0{}^i\right) \tag{2}$$

$$W_m(\mathbf{C}) = C_1\left(\tilde{I}_1 - 3\right) + K_v\left(J-1\right)^2 \tag{3}$$

$$W_{f_i}\left(\mathbf{C}, \mathbf{a}_0{}^i \otimes \mathbf{a}_0{}^i\right) = \left[C_4{}^i \Big/ \left(\alpha_4{}^i\right)^2\right]\left\{\exp\left[\alpha_4{}^i\left(I_4{}^i - 1\right)\right] - \alpha_4{}^i\left(I_4{}^i - 1\right) - 1\right\} \tag{4}$$

where $\mathbf{a}_0{}^i$ are the fibers direction, resulting from morphological characterization. The structural invariant $I_4{}^i$ is defined as $I_4{}^i = \mathbf{C}:\left(\mathbf{a}_0{}^i \otimes \mathbf{a}_0{}^i\right)$, while the constitutive parameters $C_4{}^i$ and $\alpha_4{}^i$ describes the i^{th} fibers family initial stiffness and the increase of fibers stiffness with stretch, respectively.

The discrepancy between model results and experimental data from tensile tests was evaluated by a cost function [33], whose minimization was performed by a stochastic-deterministic procedure [28,31,32]. The constitutive parameters identified were the same for the isotropic contribution of the polymeric blister and the reinforced layer (Table 2).

Table 2. Constitutive parameters of AUS cuff and the corresponding values of the cost function.

	K_v	C_1	C_4	α_4	*Cost Function*
polymeric blister	8.920 MPa	0.361 MPa	−	−	0.013
reinforced layer	8.920 MPa	0.361 MPa	6.470 MPa	1.520	0.020

Numerical analysis has been developed to simulate the inflation tests in order to validate the model developed by comparison with experimental data. A fluid-filled cavity was defined by the cuff inner surface [14,21]. Inflation process was simulated by defining a flow rate corresponding to the experimental condition. Numerical computation was performed by a HPC server equipped with two Intel Xeon E7 8890 v4 and 256 GB RAM. The analysis was developed by using 4 cpus and lasted about two hours.

3. Results

3.1. Cuff materials and morphology

During surgery, the blister of AUS cuff is positioned in contact with urethral tissues when the cuff is wrapped around the duct, while the fiber-reinforced layer is kept outwardly. The fiber-reinforced layer is based on mesh embedded in a polymeric matrix, as shown in Figure 2a. SEM analysis was carried out on the polymeric blister and on the fiber-reinforced layer. The transversal section of the fiber-reinforced layer was also observed, to get an insight on the reinforcing mesh material and conformation. The outer surface of the polymeric blister is smooth and homogeneous, while the outer surface of the fiber-reinforced layer is slightly rougher. A detail of the fiber conformation (Figure 2b,c) shows the multifilament structure of the fiber, composed by filaments with a diameter of about 30 μm. EDAX analysis was carried out to get qualitative data on

the elemental composition of the blister and fibers as shown in Figure 2d. The EDAX spectrum on the blister revealed chemical elements that are ascribable to polydimethylsiloxane (PDMS), in accordance with data reported in AMS800 technical datasheet. Differently, EDAX analysis of the fiber showed the presence of oxygen and carbon, as for several polymeric materials. Further chemical analysis was performed for a more accurate identification. Indeed, the analysis of the physicochemical properties was enhanced through FT-IR, to highlight the constituent materials. FT-IR spectra, shown in Figure 2e, confirmed that the main polymeric materials used in cuff manufacturing is PDMS [34−36]. The FT-IR spectrum of a fiber presented the main characteristic bands of polyethylene terephthalate (PET) [37−39]. This analysis provides additional data which are not commonly reported in AMS800 technical datasheet.

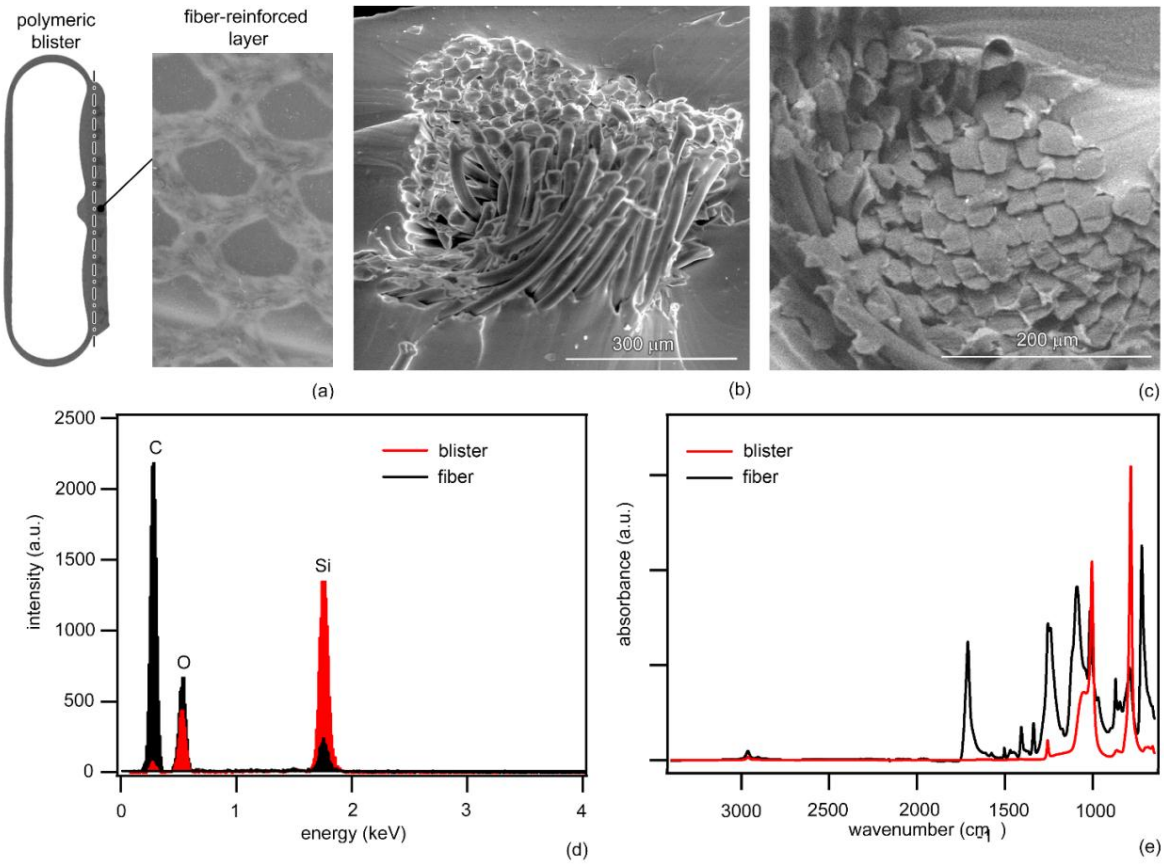

Figure 2. Scheme of a transversal section of the cuff and optical image with the reinforcing mesh (a). SEM images of cross-sections of the fiber reinforced layer (b,c). EDAX (d) and FT-IR (e) spectra acquired at cuff surface and filament regions.

CT scan provided an accurate three-dimensional geometrical model of the cuff in the deflated configuration (Figure 3a), as well as specific dimensional measurements. The software VGStudio MAX was used for the evaluation of wall-thickness and internal distance between surfaces. The wall thickness at selected sections were reported in (Figure 3b).

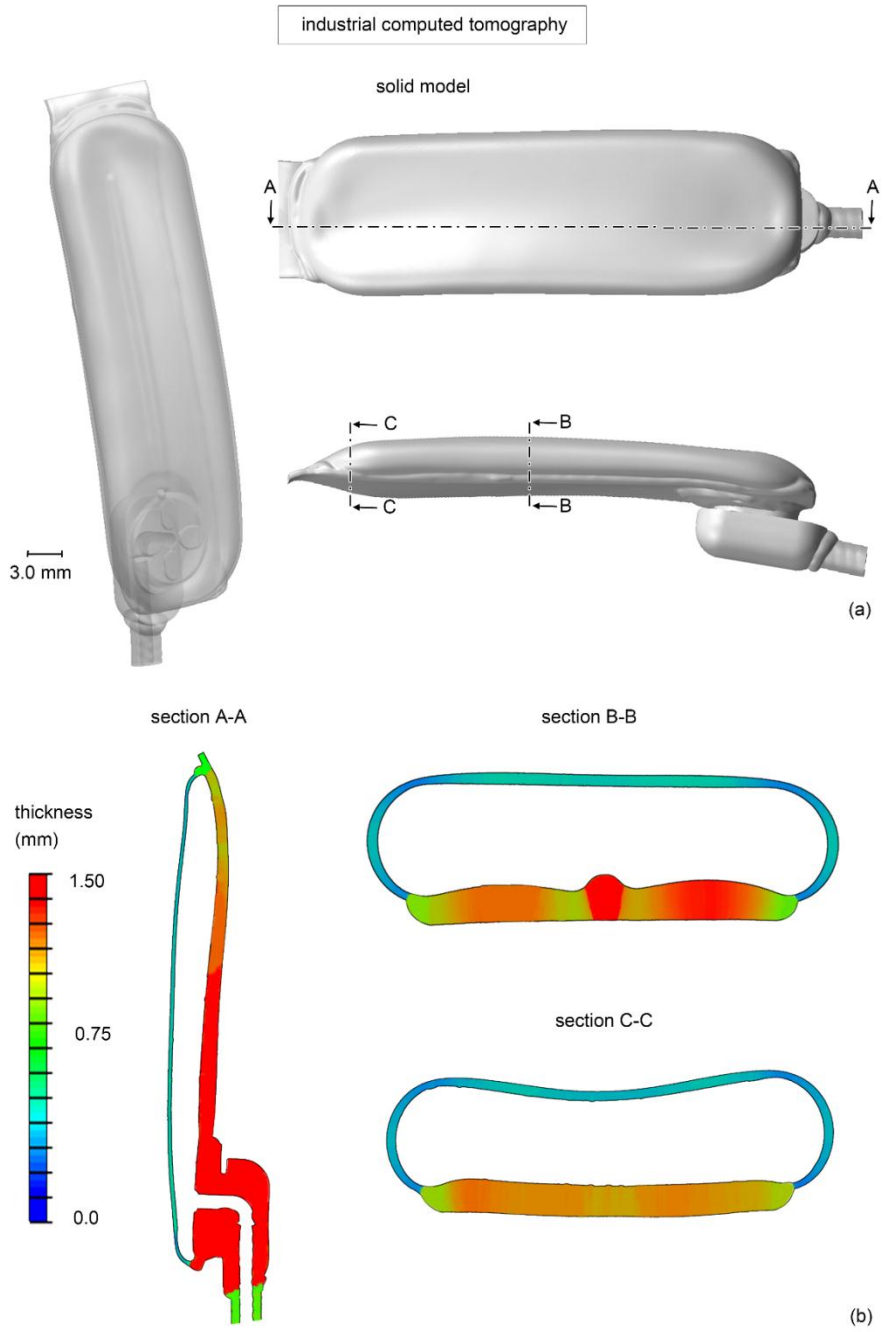

Figure 3. Computer tomographic data, as different views of the geometrical model of the cuff with indicated sections A-A, B-B and C-C (a) and contour of the material wall-thickness at the corresponding sections (b).

3.2. Mechanical properties, constitutive and numerical modeling

Results of tensile tests were reported for the cuff at the fiber-reinforced layer (Figure 4a) and the polymeric blister (Figure 4b). The fiber-reinforced layer exhibited a nonlinear mechanical behavior, with an increasing stiffness that is correlated with the reinforcement of PET network within the PDMS ground matrix. Differently, the blister was characterized by a continuous non-linear

mechanical response, with much lower stiffness. The mechanical characteristics for silicone materials can vary considerably and a sensitivity analysis was performed to investigate the effects of its variation on the overall cuff response, also considering fibers contribute. The values assumed on the specific case considered, reported by means of the constitutive material parameters, depend on average data form mechanical test associated with data in literature, but keeping in mind that the most relevant aspect, from structural point of view, is related to the geometric conformation, that was deeply investigated by CT imaging and accurately reported.

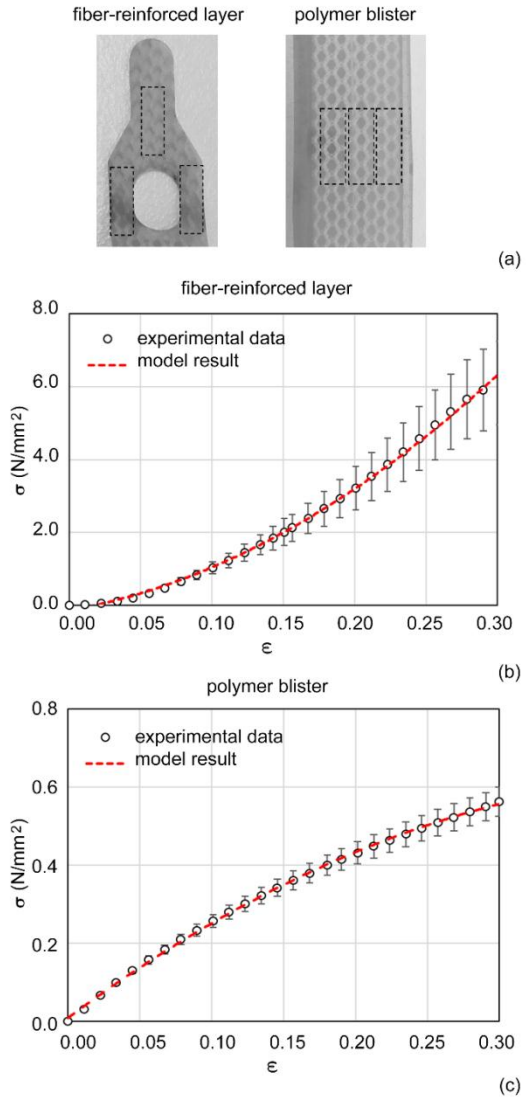

Figure 4. Position of cut samples for tensile tests from specific regions of the cuff (a). Tensile response in terms of mean nominal stress vs. nominal strain for the fiber-reinforced layer (b) and the polymer blister (c). Experimental mean data ± SD are compared with model results.

The numerical model of the cuff, obtained by the virtual solid model, was reported (Figure 5). Inflation experimental activities led to pressure data, related to the volume imposed history. The distribution of pressure vs volume data and numerical results were compared (Figure 6a), showing a

valid agreement. The maximum pressure condition was 50 cmH_2O. The contour of the displacement magnitude of the cuff was reported for the pressures of 15, 30 and 50 cmH_2O (Figure 6b). The validation of the numerical model was obtained also comparing the numerical results with the data obtained by CT scan at selected pressures (Figure 7). The internal distance between surfaces and the conformation of the cuff in the numerical model was compared by the CT scan data, at the intersection named as D-D, E-E, F-F (Figure 7) reported on section A-A (Figure 3), at 15, 30 and 50 cmH_2O. The discrepancies between the CT data and model results were reported in terms of percentage error. At section D-D the error was less than 2% while at sections E-E and F-F the error was of the order of 2.5%. The good agreement between data from experimental tests and numerical results proved the reliable interpretation of the mechanical response of the cuff.

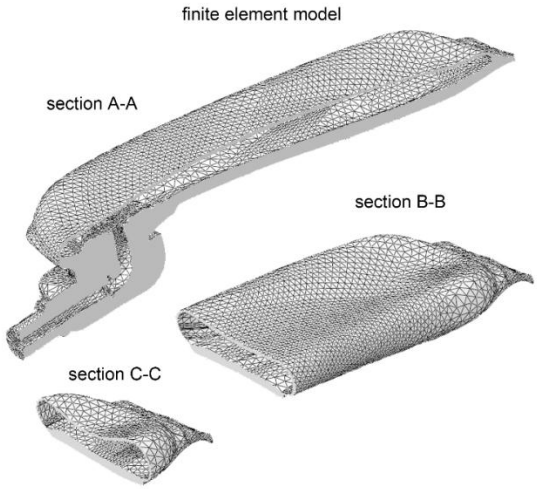

Figure 5. Finite element model of the cuff, reporting selected sections A-A, B-B and C-C, according to Figure 3.

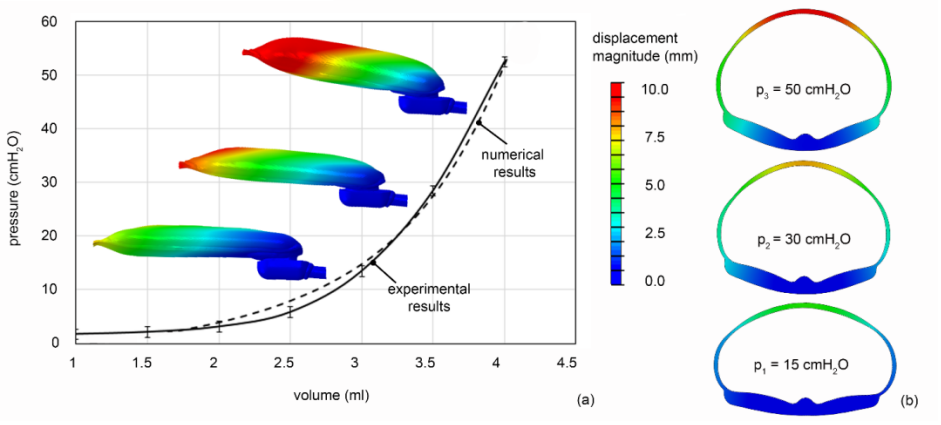

Figure 6. Comparison of experimental data (mean ± SD) and numerical results for inflation tests (a). Contour of displacement magnitude at selected pressure intensity on the section B-B (b).

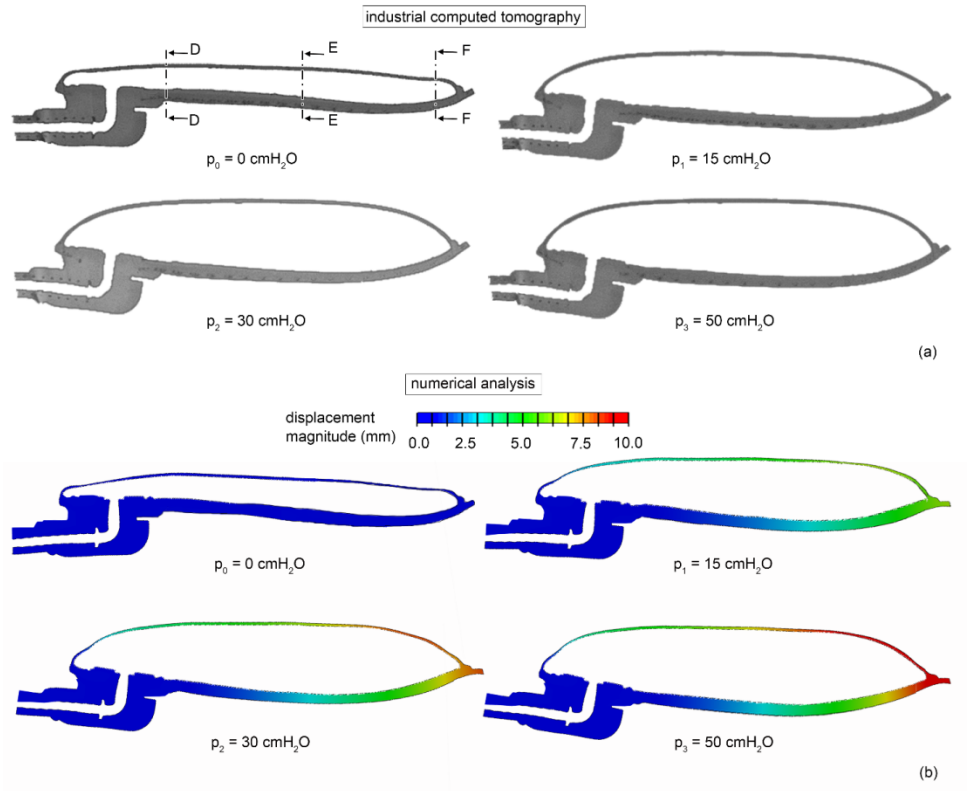

Figure 7. Validation procedure by comparison of CT data (a) and numerical results (b) during the inflation test, at selected pressure values on the section A-A. Indication of the sections D-D, E-E, F-F for the measure of the distance between internal surfaces.

4. Discussions

In this work, the experimental and computational approaches are combined to develop a finite element model of AUS cuff, aiming at providing tools for the in vitro and in silico investigation of AUS reliability during the interaction between prosthesis and urethra. The adopted procedure consists in subsequent steps including material and geometric characterization of the cuff (Figures 2–4), definition of a solid and numerical model (Figure 5) and validation by comparison of numerical results with CT images of inflated cuff (Figures 5 and 6).

The definition of the constitutive formulation developed is essential for the numerical analysis and is performed in the light of the specific experience in this area [14,25,31,33]. Results from physicochemical and mechanical testing represent a reference term for constitutive modeling. However, a limitation of this study is related to the experimental data acquired by mechanical tests, which do not take into account time-dependent behavior. Finite element discretization of the cuff that is assumed in the light of a sensitivity analysis, considering the best compromise between reducing computational cost and increasing accuracy. Model validation is achieved comparing the measurements provided by CT scanning of AUS cuff inflated at selected pressure levels and the corresponding numerical results. This approach enables to obtain a reliable numerical model able to interpret AUS cuff mechanics for in silico trials.

The approach can be applied to further artificial sphincters on the market and under

development. For example, severe fecal incontinence is generally treated by the implantation of an artificial sphincter composed of a fluid-filled cuff [41]. As for the AMS800 cuff, the geometrical and mechanical parameters are crucial and can be characterized by in silico analysis.

This work is part of extended research activities addressed to biomechanical analysis of prosthetic devices for urinary incontinence. In the frame of this topic, the urethral tissues were characterized with comprehensive experimental activities and numerical modelling [12,26,28]. To consider ageing and pathological conditions, a specific investigation has been carried out evaluating different urethral tissue conditions, in accordance with variable stiffness [40,42].

The interaction between urethra and AUS cuff has been studied by means of computational analysis to identify the AUS pressure that ensures lumen occlusion and the stress distributions within biological tissues [14,21]. This investigation entails a detailed knowledge of AUS conformation and mechanics achieved through experimental characterization and numerical modelling, as here presented. In this work, only AMS 800 is considered, but also other AUS devices can be studied with the same approach. Moreover, nevertheless the main application of AUS devices pertain to adulty male subjects, the investigation of AUS can be extended to other patients, considering the number of females and children that have obtained AUS [43,44]. Despite some limitations, this study offers a valid basis for the comprehension of AUS cuff behavior and the development of computational analysis of AUS cuff associated to urethral duct.

Acknowledgments

This study has been supported by University of Padova, Project n ° CPDA148900/14, titled COMPUR: Definition of COMPutational tools for the analysis of the biomechanical functionality of the lower URinary system.

Conflict of interest

The authors declare no conflict of interest in this paper.

References

1. A. D. Markland, P. S. Goode, D. T. Redden, L. G. Borrud, K .L. Burgio, Prevalence of urinary incontinence in men: Results from the national health and nutrition examination survey, *J. Urol.*, **184** (2010), 1022–1027.
2. I. Milsom, K. S. Coyne, S. Nicholson, M. Kvasz, C. I. Chen, A. J. Wein, Global prevalence and economic burden of urgency urinary incontinence: A systematic review, *Eur. Urol.*, **65** (2014), 79–95.
3. B. H. Cordon, N. Singla, A. K. Singla, Artificial urinary sphincters for male stress urinary incontinence: Current perspectives, *Med. Devices. (Auckl)*, **9** (2016), 175–183.
4. B. S. Malaeb, S. P, Elliott, J. Lee, D. W. Anderson, G. W. Timm, Novel artificial urinary sphincter in the canine model: The tape mechanical occlusive device, *Urology*, **77** (2011), 211–216.
5. C. C. Carson, Artificial urinary sphincter: Current status and future directions, *Asian J. Androl.*, **22** (2020), 154−157.

6. P. Weibl, R. Hoelzel, M. Rutkowski, W. Huebner, VICTO and VICTO-plus–novel alternative for the management of postprostatectomy incontinence, early perioperative and postoperative experience, *Cent. Eur. J. Urol.*, **71** (2018), 248–249.
7. T. A. Ludwig, P. Reiss, M. Wieland, A. Becker, M. Fisch, F. K. Chun, et al. The ARTUS device: The first feasibility study in human cadavers, *Can. J. Urol.*, **22** (2015), 8100–8104.
8. C. A. Hajivassiliou, A review of the complications and results of implantation of the AMS artificial urinary sphincter, *Eur. Urol.*, **35** (1999), 36–44.
9. A. C. J. Santos, L .O. Rodrigues, D. C. Azevedo, L. M. Carvalho, M. R. Fernandes, S. O. Avelar, et al., Artificial urinary sphincter for urinary incontinence after radical prostatectomy: A historical cohort from 2004 to 2015, *Int. Braz. J. Urol.*, **43** (2017), 150–154.
10. E. Chung, A state-of-the-art review on the evolution of urinary sphincter devices for the treatment of post-prostatectomy urinary incontinence: Past, present and future innovations, *J. Med. Eng. Technol.*, **38** (2014), 328–332.
11. A. N. Natali, E. L. Carniel, A. Frigo, P. G. Pavan, S. Todros, P. Pachera, et al., Experimental investigation of the biomechanics of urethral tissues and structures, *Exp. Physiol.*, **101** (2016), 641–656.
12. A. N. Natali, E. L. Carniel, C. G. Fontanella, A. Frigo, S. Todros, A. Rubini, et al., Mechanics of the urethral duct: tissue constitutive formulation and structural modeling for the investigation of lumen occlusion, *Biomech. Model Mechanobiol.*, **16** (2017), 439–447.
13. F. Marti, T. Leippold, H. John, N. Blunschi, B. Muller, Optimization of the artificial urinary sphincter: modelling and experimental validation, *Phys. Med. Biol.*, **51** (2006), 1361.
14. A. N. Natali, E. L. Carniel, C. G. Fontanella, Interaction phenomena between a cuff of an artificial urinary sphincter and a urethral phantom, *Artif. Organs.*, **43** (2019), 888–896.
15. L. De Chiffre, S. Carmignato, J. P. Kruth, R. Schmitt, A. Weckenmann, Industrial applications of computed tomography, *CIRP. Ann. Manuf. Techn.*, **63** (2014), 655–677.
16. J. P. Kruth, M. Bartscher, S. Carmignato, R. Schmitt, L. De Chiffre, A. Weckenmann, Computed tomography for dimensional metrology, *CIRP Ann. Manuf. Techn.*, **60** (2011), 821–842.
17. M. Sacher G. Schulz, H. Deyle, K. Jager, B. Muller, Comparing the accuracy of intraoral scanners, using advanced micro computed tomography, *Proc. SPIE*, **11113** (2019), 111131Q.
18. B. Müller, Recent trends in high-resolution hard x-ray tomography, *Proc. SPIE*, **11113** (2019), 1111302.
19. J. Von Jackowski, G. Schulz, B. Osmani, T. Töpper, B. Müller, Three-dimensional characterization of soft silicone elements for intraoral device, *Proc. SPIE*, **11113** (2019), 1111314.
20. C. Vogtlin, G. Schulz, K. Jager, B. Muller, Comparing the accuracy of master models based on digital intra-oral scanners with conventional plaster casts, *Phys. Med.*, **1** (2016), 20–26.
21. A. N. Natali, C. G. Fontanella, E. L. Carniel, Biomechanical analysis of the interaction phenomena between artificial urinary sphincter and urethral duct, *Int. J. Numer. Meth. Bio.*, **36** (2020), e3308.
22. S. Affatato, F. Zanini, S. Carmignato, Quantification of wear and deformation in different configurations of polyethylene acetabular cups using micro X-ray computed tomography, *Materials*, **10** (2017), 259.
23. L. A. Feldkamp, L. C. Davis, J. W. Kress, Practical cone-beam algorithm, *J. Opt. Soc. Am. A*, **1** (1984), 612–619.

24. S. Carmignato, V. Aloisi, F. Medeossi, F. Zanini, E. Savio, Influence of surface roughness on computed tomography dimensional measurements, *CIRP Ann. Manuf. Techn.*, **66** (2017), 499–502.
25. E. L. Carniel, V. Gramigna, C. G. Fontanella, C. Stefanini, A. N. Natali, Constitutive formulation for the mechanical investigation of colonic tissues, *J. Biomed. Mat. Res. Part A*, **102** (2014), 1243–1254.
26. A. N. Natali, E. L. Carniel, C. G. Fontanella, S. Todros, G. M. De Benedictis, M. Cerruto, et al., Urethral lumen occlusion by artificial sphincteric devices: A computational biomechanics approach, *Biomech. Model Mechanobiol.*, **16** (2017), 1439–1446.
27. E. L. Carniel, A. Frigo, C. G. Fontanella, G. M. De Benedictis, A. Rubini, L. Barp, et al., A biomechanical approach to the analysis of methods and procedures of bariatric surgery, *J. Biomech.*, **56** (2017), 32–41.
28. A. N. Natali, E. L. Carniel, A. Frigo, C. G. Fontanella, A. Rubini, Y. Avital, et al., Experimental investigation of the structural behavior of equine urethra, *Comput. Methods Programs Biomed.*, **141** (2017), 35–41.
29. *Abaqus Documentation, Version 6.14-2*, Dassault Systémes Simulia Corp., Providence, RI, 2014. Available from: http://www.130.149.89.49:2080/v6.11/index.html.
30. A. N. Natali, C. G. Fontanella, E. L. Carniel, A numerical model for investigating the mechanics of calcaneal fat pad region, *J. Mech. Behav. Biomed. Mat.*, **5** (2012), 216–223.
31. C. G. Fontanella, E. L. Carniel, A. Forestiero, A. N. Natali, Investigation of the mechanical behaviour of foot skin, *Skin Res. Tech.*, **20** (2014), 445–452.
32. E. L. Carniel, V. Gramigna, C. G. Fontanella, A. Frigo, C. Stefanini, A. Rubini, et al., Characterization of the anisotropic mechanical behaviour of colon tissues: Experimental activity and constitutive formulation, *Exp. Physiol.*, **99** (2014), 759–771.
33. A. N. Natali, A. Audenino, W. Artibani, C.G. Fontanella, E.L. Carniel, E.M. Zanetti, Bladder tissue biomechanical behaviour: Experimental tests and constitutive formulation, *J. Biomech.*, **48** (2015), 3088–3096.
34. E. A. Romanenko, B. V. Tkachuk, Infrared spectra and structure of thin polydimethylsiloxane films, *J. Appl. Spectrosc.*, **18** (1973), 188–192.
35. K. Chamerski, M. Lesniak, M. Sitarz, M. Stopa, J. Filipecki, An investigation of the effect of silicone oil on polymer intraocular lenses by means of PALS, FT-IR and Raman spectroscopies, *Spectrochim. Acta A*, **167** (2016), 96–100.
36. L. M. Johnson, L. Gao, I. V. Shields, M. Smith, K. Efimenko, K. Cushing, et al., Elastomeric microparticles for acoustic mediated bioseparations, *J. Nanobiotechnol.*, **28** (2013), 22.
37. M. C. Tobin, The infrared spectra of polymers. II. The infrared spectra of polyethylene terephthalate, *J. Phys. Chem. US*, **61** (1957), 1392–1400.
38. C. Y. Liang, S. Krimm, Infrared spectra of high polymers: Part IX. Polyethylene terephthalate, *J. Mol. Spectrosc.*, **3** (1959), 554–574.
39. A. A. Ouroumiehei, I. G. Meldrum, Characterization of polyethylene terephthalate and functionalized polypropylene blends by different methods, *Iran Polym. J.*, **8** (1999), 193–204.
40. A. N. Natali, C. G. Fontanella, S. Todros, E. L. Carniel, Urethral lumen occlusion by artificial sphincteric device: Evaluation of degraded tissues effects, *J. Biomech.*, **64** (2017), 75–81.

41. E. Fattorini, T. Brusa, C. Gingert, S. E. Hieber, V. Leung, B. Osmani, et al., Artificial muscle devices: Innovations ad prospects for fecal incontinence treatment, *Annals Biomed. Eng.*, **44** (2019), 1355–1369.
42. A. N. Natali, E. L. Carniel, C. G. Fontanella, Investigation of interaction phenomena between lower urinary tract and artificial urinary sphincter in consideration of urethral tissues degeneration, *Biomech. Model Mechanobiol.*, 2020. Available from: https://link.springer.com/article/10.1007%2Fs10237-020-01326-3.
43. E. Ruiz, J. Puigdevall, J. Moldes, P. Lobos, M. Boer, J. Ithurralde, et al., 14 years of experience with the artificial urinary sphincter in children and adolescent without spina bifida, *J. Urol.*, **176** (2006), 1821–1825.
44. M. Islah, S. Y. Cho, H. Son, The current role of the artificial urinary sphincter in male and female urinary incontinence, *World J. Mens. Health.*, **31** (2013), 21–30.